Supporting Information

Collaborative Reconstruction of FeOOH/FeNiCo-LDH Heterogeneous Nanosheets for Enhancing Anion Exchange Membrane Seawater Electrolysis

Yixing Luo,[a] Yang Yang,[b] Yakun Tian,[a] Qingsheng Wu,[a] Wen-Feng Lin[b] and Ming Wen*[a]

[a] School of Chemical Science and Engineering, Shanghai Key Laboratory of Chemical Assessment and Sustainability, Tongji University, Shanghai, 200092, China

[b] Department of Chemical Engineering, Loughborough University, Loughborough, Leicestershire, LE11 3TU, UK.

* Corresponding author: Ming Wen (Email: m_wen@tongji.edu.cn)

Experimental section

Fabrication of ZIF-67 and FeOOH/FeNiCo-LDH

Typically, 30 mL CH_3OH containing 2.0 mmol $Co(NO_3)_2 \cdot 6H_2O$ was mixed with 30 mL CH_3OH containing 8.0 mmol 2-MeIm for 6 h at room temperature to generate ZIF-67. Then, FeOOH/FeNiCo-LDH was prepared according to the similar experimental procedures of FeOOH/FeNiCo-LDH/HCNC, except with the ZIF-67 as precursor.

Fabrication of NiCo-LDH/HCNC

NiCo-LDH/HCNC was prepared according to the similar synthesis procedure of FeOOH/FeNiCo-LDH/HCNC, except without the addition of $FeCl_2 \cdot 4H_2O$.

Characterization

X-ray diffraction (XRD) patterns were collected using the Bruker D8 advanced X-ray diffractometer with a Cu Kα radiation. Scanning electron microscope (SEM, JEOL, S4800) and transmission electron microscope (TEM, JEOL, JEM-2100EX) were used to investigate microstructures of the as-prepared samples. Nitrogen adsorption-desorption isotherms were obtained using the Micromeritics ASAP 3020 instruments operated at 77 K. X-ray photoelectron spectroscope (XPS) analyses were operated using a Thermo Scientific ESCALAB 250Xi X-ray photoelectron spectrometer with an Al Kα source. Inductively coupled plasma-optical emission spectrometry (ICP-OES) was recorded on Perkinelmer ICP Optima 8300 (PE ICP 8300). Raman spectra were obtained using a RENISHAW Via Raman Microscope with the excitation source of

laser wavelength of 514 nm. *In-situ* Raman spectra were collected on a Horiba LabRAM HR Evolution with the excitation source of laser wavelength of 532 nm. *In-situ* Raman measurements were carried out in a custom-made spectro-electrochemical cell under controlled potentials. A Hg/HgO and a graphite rod were used as reference electrode and counter electrode, respectively.

DFT calculations

Structural models of FeOOH/FeNiCo-LDH, FeNiCoOOH, NiCo-LDH, and NiCoOOH were constructed for DFT calculations. NiCo-LDH was constructed based on Ni-LDH (002). Three OH vacancies were introduced to expose reactive sites and four hydrogen atoms were removed on surface to maintain balance of valence electrons. (Lattice parameters of NiCo-LDH: a = 12.25612Å, b = 10.52013Å, c = 24.50260Å). NiCoOOH was constructed based on *β*-FeOOH (200). Fe atoms were replaced with Ni atoms, then one Ni atom was replaced with Co atom. Twelve oxygen vacancies were introduced to maintain balance of valence electrons. (Lattice parameters of NiCoOOH: a = 12.049482Å, b = 10.325105Å, c = 30.000Å). FeNiCoOOH was constructed based on *β*-FeOOH (200). Twelve oxygen vacancies were introduced to maintain balance of valence electrons. (Lattice parameters of FeNiCoOOH: a = 12.154175Å, b = 10.155464Å, c = 30.000Å). FeOOH/FeNiCo-LDH heterostructure was constructed based on FeOOH (200) and FeNiCo-LDH (002). Then one Ni atom was replaced with Co atom. Three OH vacancies were introduced to expose reactive sites and seven hydrogen atoms were removed on surface to maintain balance of valence electrons.

(Lattice parameters of FeOOH/FeNiCo-LDH: a = 12.203786Å, b = 10.380383Å, c = 30.000Å).

Structural optimization was performed by Vienna Ab-initio Simulation Package (VASP) with the projector augmented wave (PAW) method **[S1, S2]**. The exchange-functional was treated using the Perdew-Burke-Ernzerhof (PBE) functional, in combination with the DFT-D3 correction **[S3, S4]**. Cut-off energy of the plane-wave basis was set as 450 eV. For optimization of both geometry and lattice size, the Brillouin zone integration was performed with Monkhorst-Pack k-point sampling of 2×2×1 **[S5]**. The self-consistent calculations applied a convergence energy threshold of 10^{-5} eV. The equilibrium geometries and lattice constants were optimized with maximum stress on each atom within 0.02 eV $Å^{-1}$. The spin polarization method was adopted to describe magnetism of structural models. Isosurface level of charge density difference of FeOOH/FeNiCo-LDH was set at 0.02 e $Å^{-3}$. The Hubbard U correction was added to describe strong interactions of 3d orbitals, where U_{Fe} = 4.0 eV, U_{Ni} = 6.4 eV, U_{Co} = 3.3 eV **[S6-S8]**.

The adsorption model by employing the computational hydrogen electrode (CHE) model was adopted for the calculation of Gibbs free energy **[S9]**. The Gibbs free energy of H atom was calculated according to ½ $H_2 \rightarrow H^+ + e^-$, where $G(H^+) = ½ G(H_2)$. And the dehydrogenation process of NiCo-LDH was described as single site pathway:

$$*H + OH^- (aq) \rightarrow *H\text{-vacancy} + H_2O (l)$$

Elementary steps of OER on FeNiCoOOH and NiCoOOH were described as dual sites pathway **[S10]**:

$$* + OH^- (aq) \rightarrow *OH + e^-$$

$$*OH + OH^- (aq) \rightarrow *O + H_2O (aq) + e^-$$

$$*O + OH^- (aq) \rightarrow *Ov\text{-}OH + O_2 (aq) + e^-$$

$$*Ov\text{-}OH + OH^- (aq) \rightarrow * + H_2O (l) + e^-$$

In the above reactions, * represents the bare surface of structural models. *i represents the surface of structural models adsorbing intermediate i. Gibbs free energy of intermediate i was calculated as G = E + G(T) + 0.0592 pH - eU. E represents the total energy of structural models. G(T) represents the thermal correction of Gibbs free energy of *i. Kelvin temperature T was set at 298.15 K. The applied potentials U was set at 0 and 1.23 V. Gibbs free energy of OH^- and O_2 in their aqueous phase were obtained based on standard molar free energy of formation and standard hydrogen electrode (SHE) **[S11]**. G(T) of *i was obtained by VASPKIT interface **[S12]**.

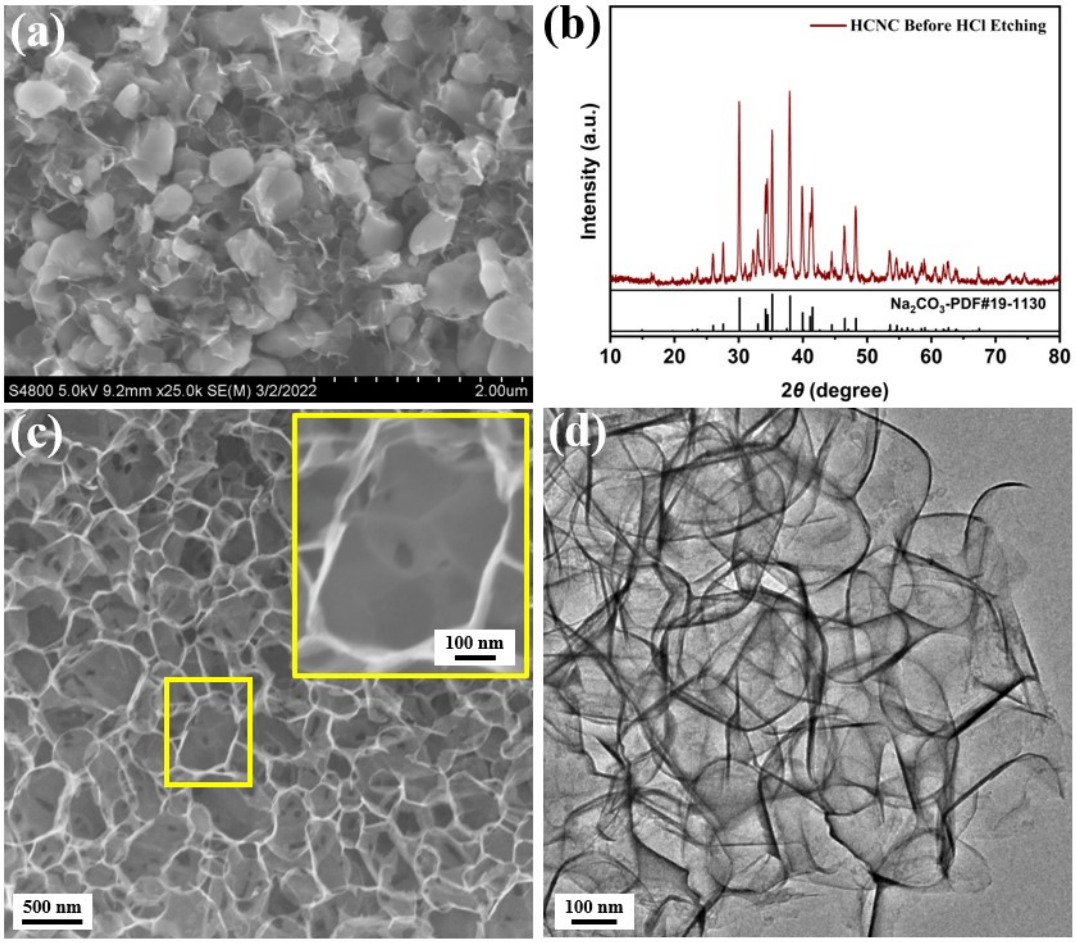

Fig. S1. (a) SEM image and (b) XRD pattern of HCNC before HCl etching. (c) SEM image and (d) TEM image of HCNC.

HCNC displays typical honeycomb-channel structure with plenty mesoporous on the carbon wall to connect each cavity, which is favorable for facilitating the mass transfer efficiency during electrochemical reaction.

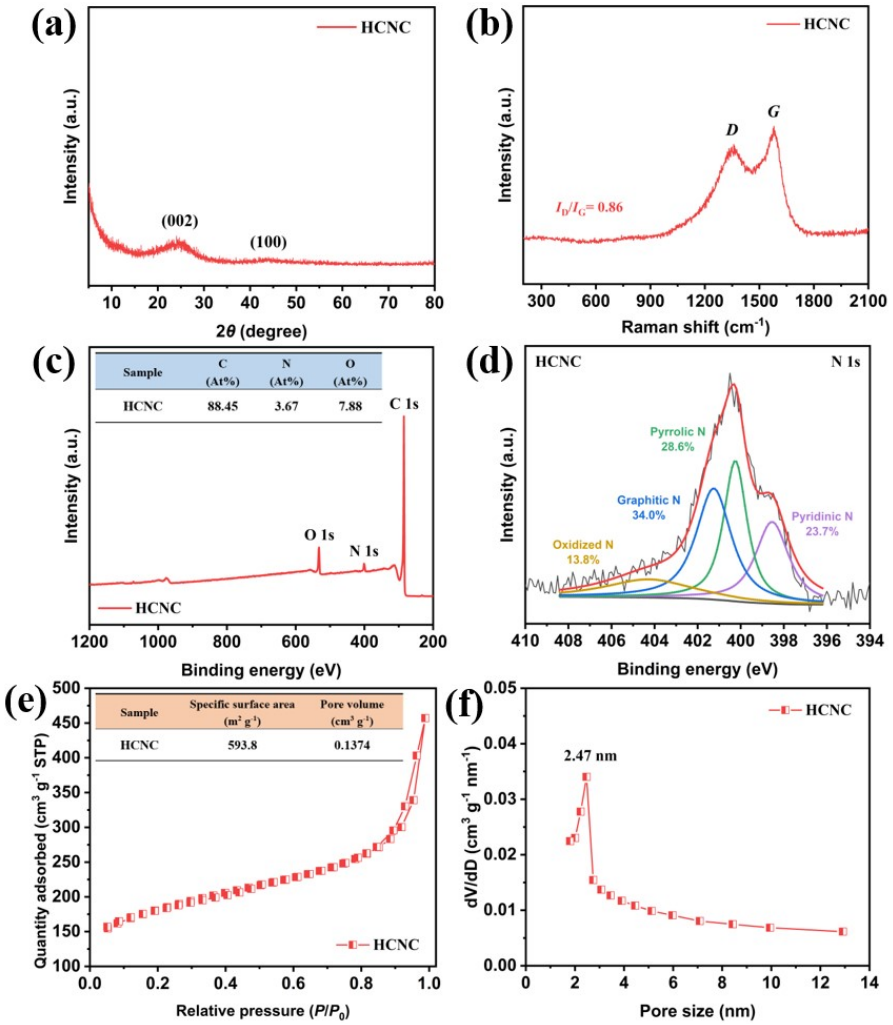

Fig. S2. (a) XRD pattern, (b) Raman spectra, and (c) Survey XPS spectra of HCNC. (d) High-resolution XPS spectra of N 1s in HCNC. (e) Nitrogen adsorption-desorption isotherms and (f) corresponding pore diameter distribution curves of HCNC.

HCNC presents two broad diffraction peaks centered around 2θ = 25° and 44° corresponding to the (002) and (100) plane of graphite carbon **(Fig. S2a)**, respectively. Raman spectra **(Fig. S2b)** further confirm the high graphitization degrees of HCNC (I_D/I_G = 0.86), which is favorable for enhancing the electron migrate capacity during electrochemical reaction.

HCNC is composed of C (284.8 eV), N (400.5 eV), and O (532.2 eV) **(Fig. S2c)**. And the deconvoluted peak of N 1s is divided into pyridinic N (398.5 eV), pyrrolic N (400.3 eV), graphitic N (401.3 eV), and oxidized N (404.3 eV) species **(Fig. S2d)**, respectively. The multifarious nitrogen species and abundant nitrogen content (3.67 At%) provide numerous C-N_x sites for the stabilization of fish scale-like FeOOH/FeNiCo-LDH nanosheets on HCNC substrates.

HCNC possesses large specific surface areas of 593.8 cm^2 g^{-1} and rich mesopores of 2.47 nm **(Fig. S2e and Fig. S2f)**, which provides numerous available sites for the stabilization of fish scale-like FeOOH/FeNiCo-LDH nanosheets.

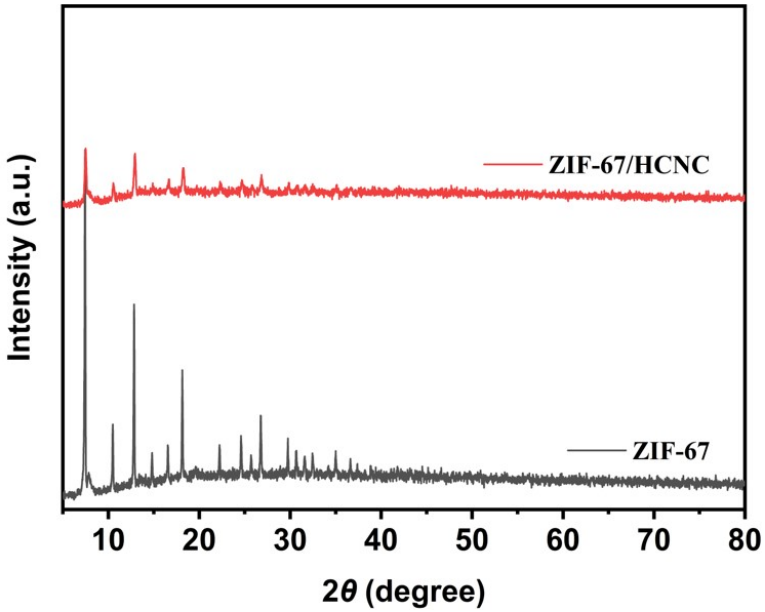

Fig. S3. XRD patterns of ZIF-67 and ZIF-67/HCNC.

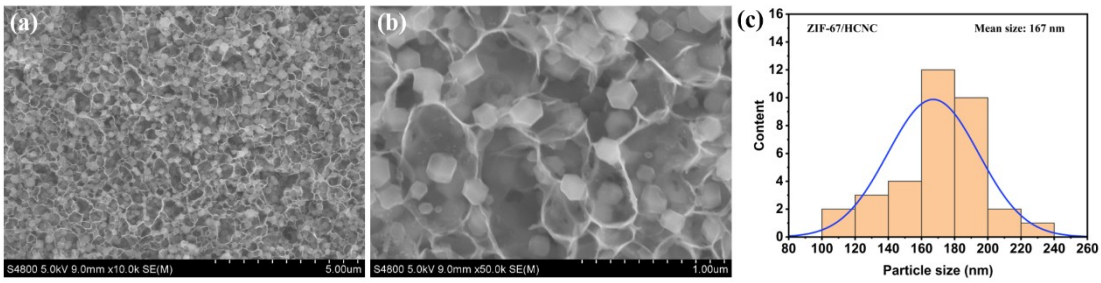

Fig. S4. (a, b) SEM images and (c) ZIF-67 size distribution of ZIF-67/HCNC.

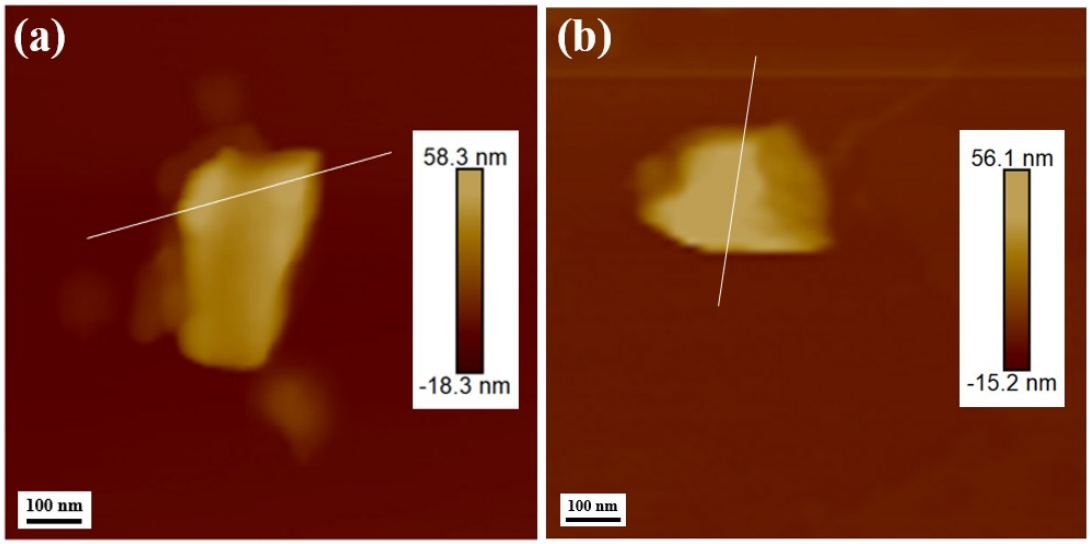

Fig. S5. Atomic force microscope image of (a) FeOOH/FeNiCo-LDH/HCNC and (b) HCNC.

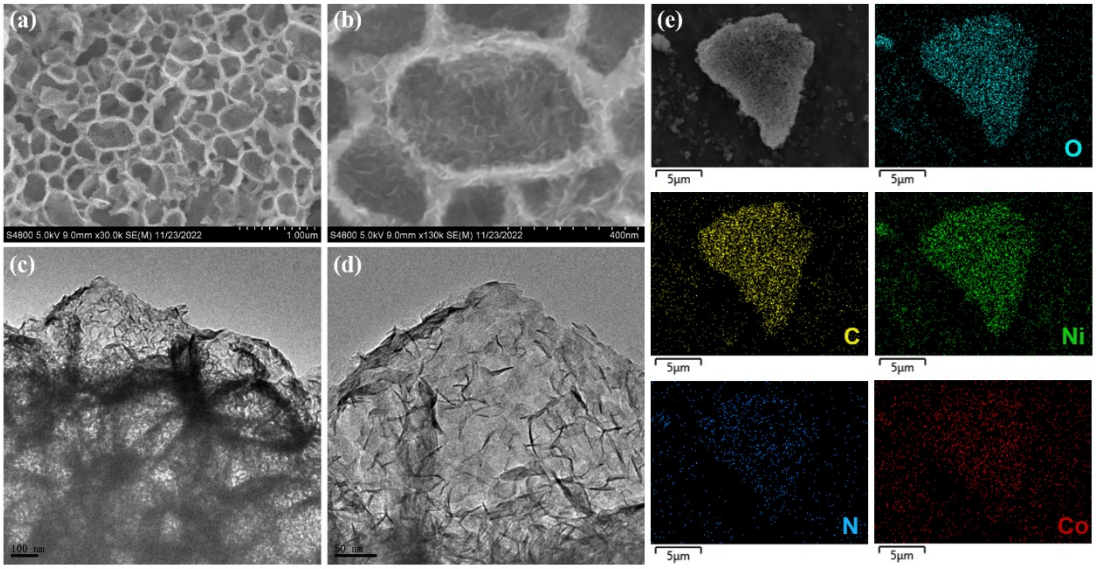

Fig. S6. (a, b) SEM images, (c, d) TEM images, and (e) Elemental mappings of NiCo-LDH/HCNC.

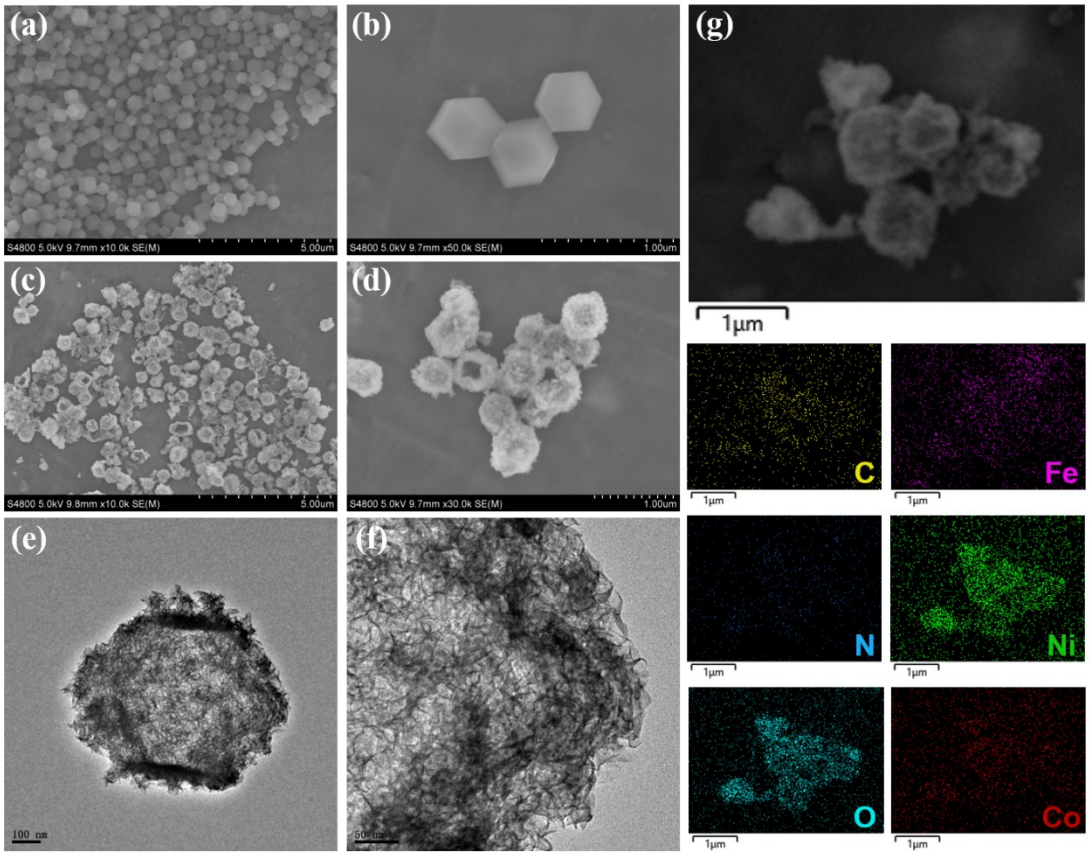

Fig. S7. (a, b) SEM images of ZIF-67. (c, d) SEM images, (e, f) TEM images, and (g) Elemental mappings of FeOOH/FeNiCo-LDH.

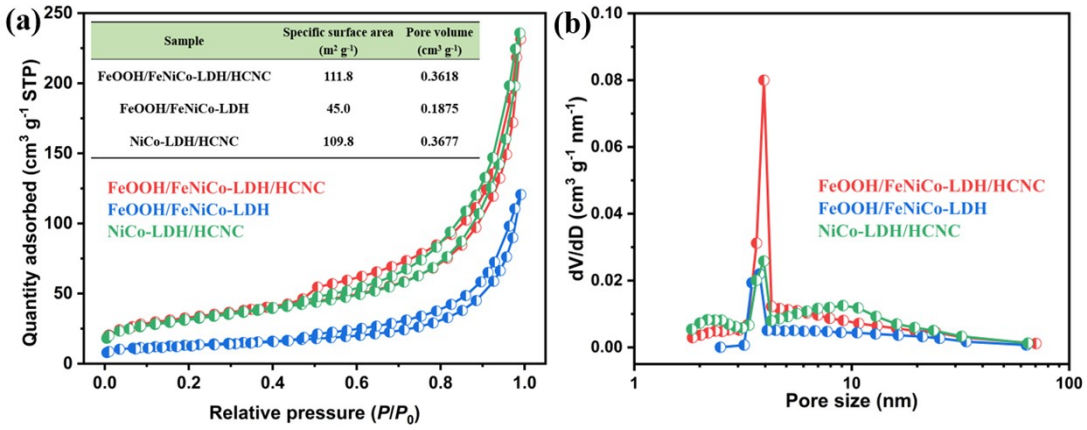

Fig. S8. (a) Nitrogen adsorption-desorption isotherms and (b) corresponding pore diameter distribution curves of FeOOH/FeNiCo-LDH/HCNC and its comparative samples.

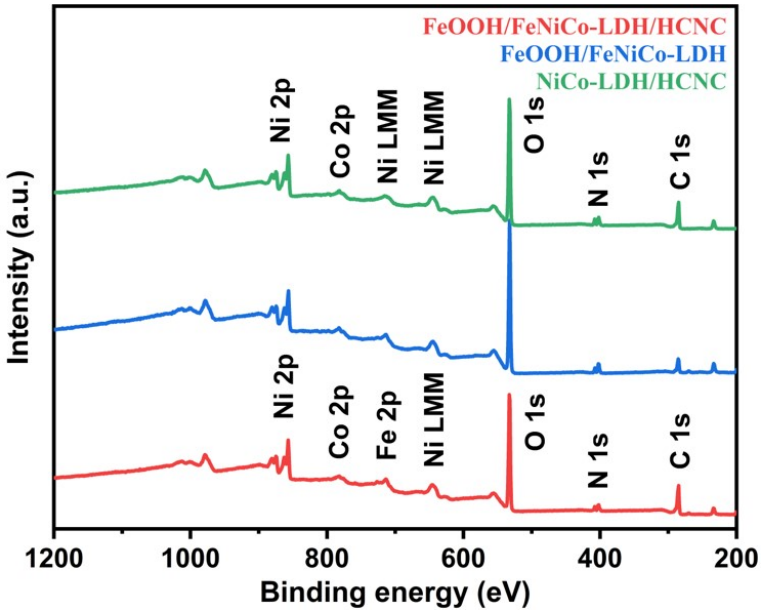

Fig. S9. Survey XPS spectra of FeOOH/FeNiCo-LDH/HCNC and its comparative samples.

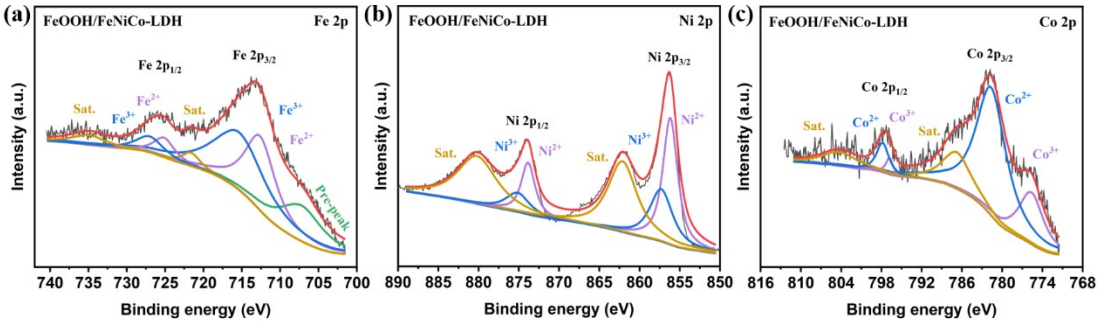

Fig. S10. High-resolution XPS spectra of (a) Fe 2p (b) Ni 2p, and (c) Co 2p in FeOOH/FeNiCo-LDH.

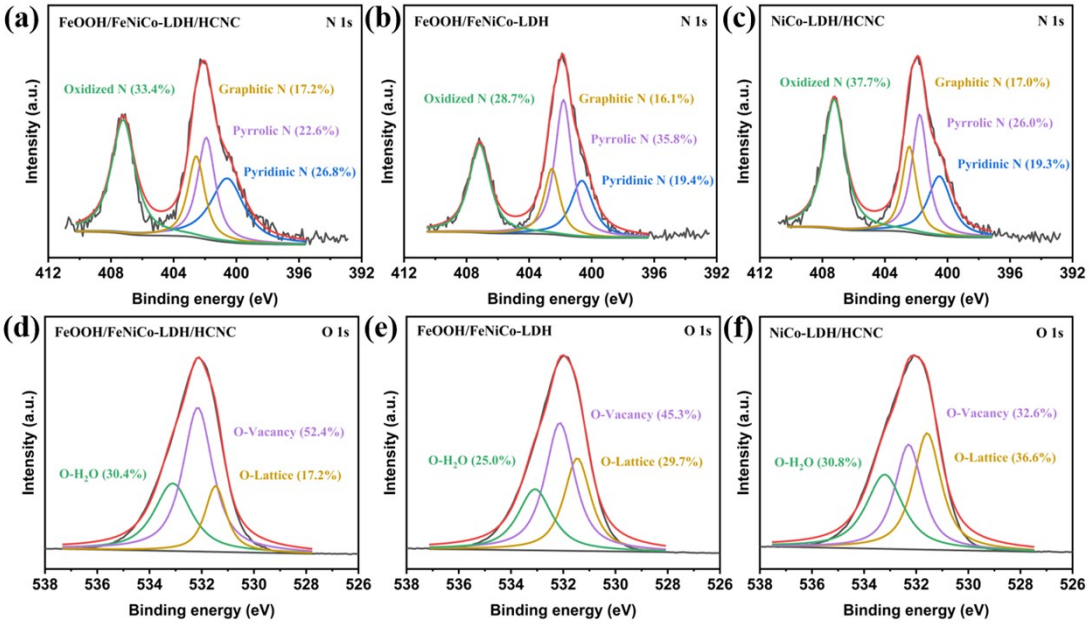

Fig. S11. High-resolution XPS spectra of (a-c) N 1s and (d-f) O 1s in FeOOH/FeNiCo-LDH/HCNC and its comparative samples.

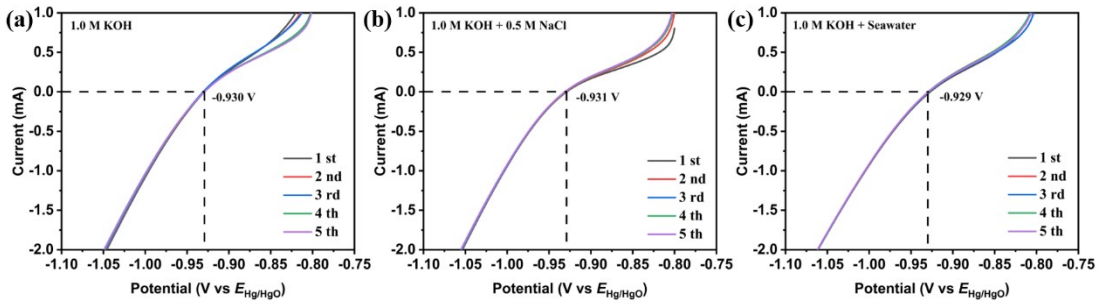

Fig. S12. LSV curves for the calibration of Hg/HgO reference electrode in (a) 1.0 M KOH, (b) 1.0 M KOH + 0.5 M NaCl, and (c) 1.0 M KOH + seawater.

For the conversion of electrode potentials quoted against the reversible hydrogen electrode (RHE), the reference electrode employed in the experiments was experimentally calibrated with respect to RHE. The calibration was conducted in the high-purity hydrogen saturated electrolytes (1.0 M KOH, 1.0 M KOH + 0.5 M NaCl, and 1.0 M KOH + seawater) with a Pt wire as the working electrode and a Pt foil as the counter electrode. LSV curves were performed at a scan rate of 1 mV s^{-1} for five times **(Fig. S12)**, and the average of the five potentials at which the current crossed zero was taken to be the thermodynamic potential for the hydrogen electrode reactions, and the following equation was applied:

For 1.0 M KOH:

$$E_{RHE} = E_{Hg/HgO} + 0.930\ V$$

For 1.0 M KOH + 0.5 M NaCl:

$$E_{RHE} = E_{Hg/HgO} + 0.931\ V$$

For 1.0 M KOH + seawater:

$$E_{RHE} = E_{Hg/HgO} + 0.929\ V$$

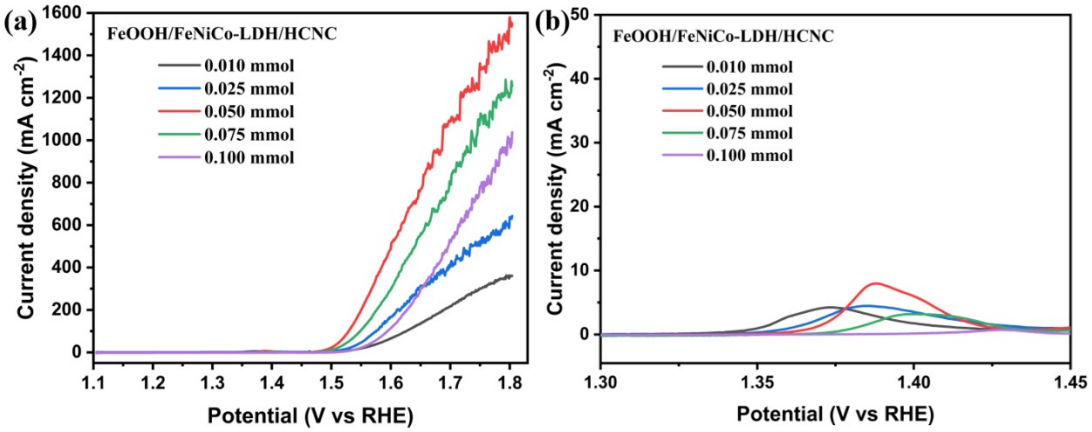

Fig. S13. (a) LSV curves and (b) corresponding enlarged LSV curves for OER in 1.0 M KOH of FeOOH/FeNiCo-LDH/HCNC prepared with different Fe^{2+} dosage.

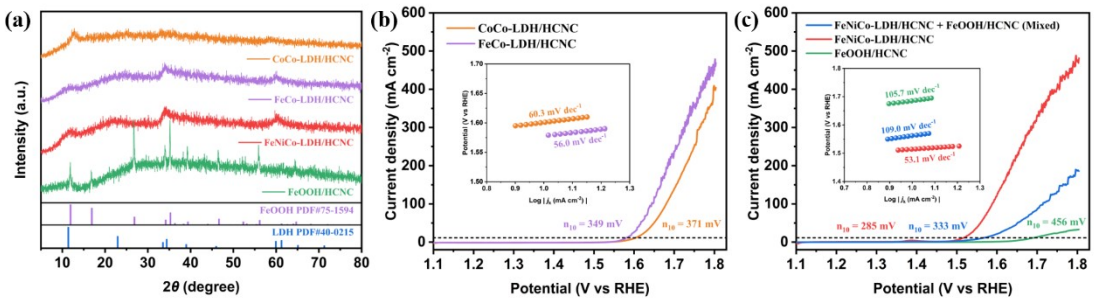

Fig. S14. (a) XRD pattern and (b, c) LSV curves for OER in 1.0 M KOH of different samples.

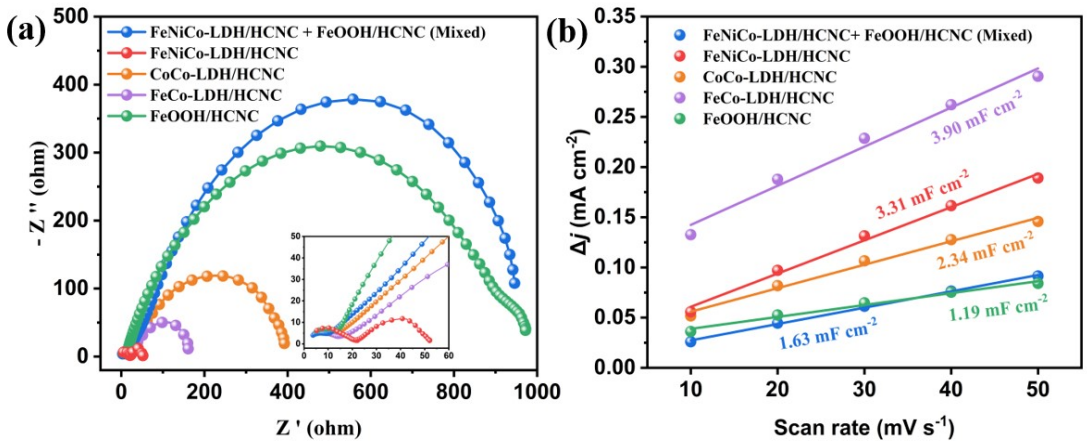

Fig. S15. (a) C_{dl} values and (b) Nyquist plots of CoCo-LDH/HCNC, FeCo-LDH/HCNC, FeNiCo-LDH/HCNC, FeOOH/HCNC, and FeNiCo-LDH/HCNC+FeOOH/HCNC (Mixed).

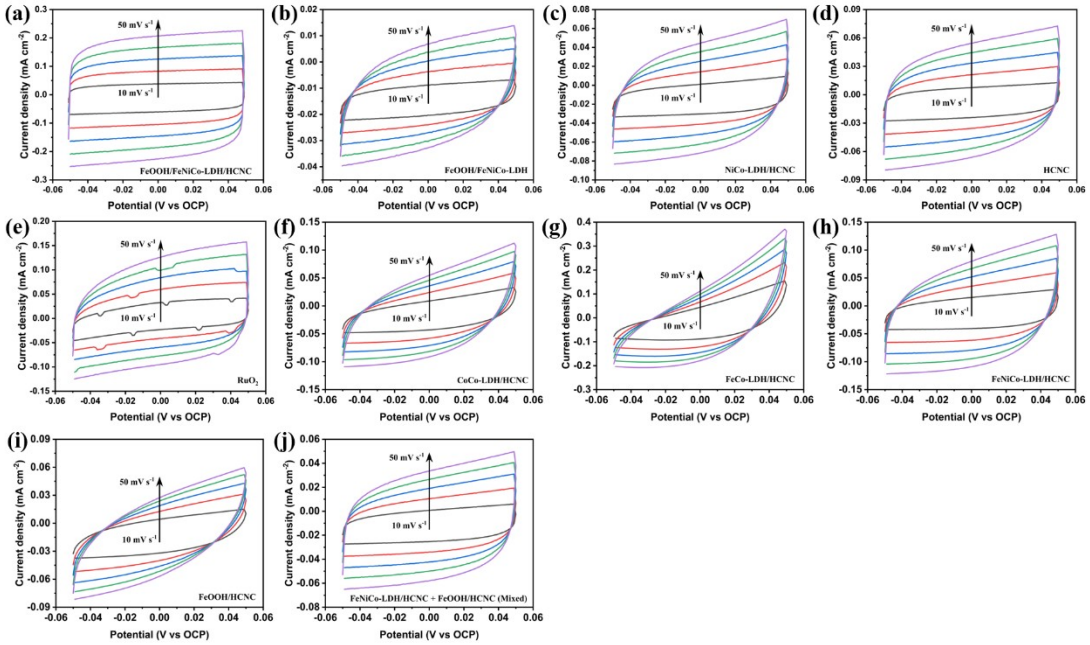

Fig. S16. CV curves in non-Faradic region at different scan rates from 10 to 50 mV s^{-1} of (a) FeOOH/FeNiCo-LDH/HCNC, (b) FeOOH/FeNiCo-LDH, (c) NiCo-LDH/HCNC, (d) HCNC, (e) RuO_2, (f) CoCo-LDH/HCNC, (g) FeCo-LDH/HCNC, (h) FeNiCo-LDH/HCNC, (i) FeOOH/HCNC, and (j) FeNiCo-LDH/HCNC+FeOOH/HCNC (Mixed).

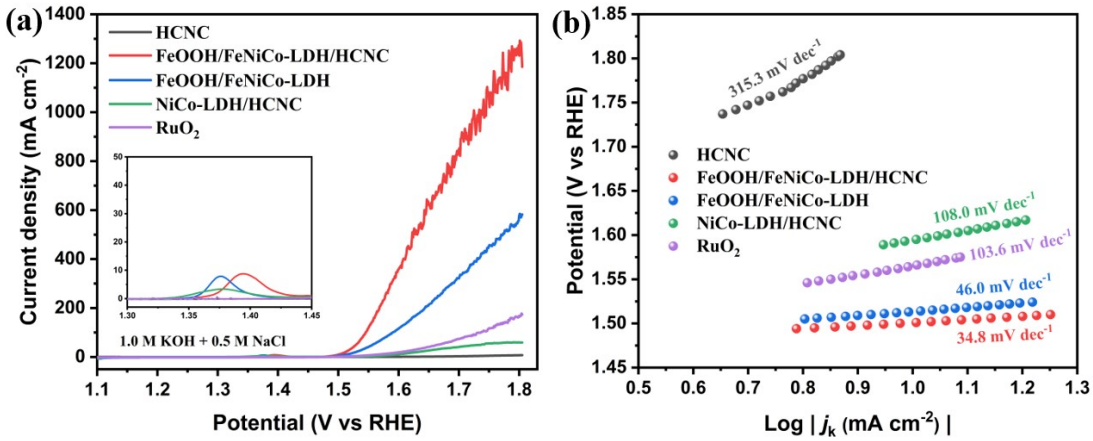

Fig. 17. (a) LSV curves and (b) corresponding Tafel plots for OER in 1.0 M KOH + 0.5 M NaCl of FeOOH/FeNiCo-LDH/HCNC and its comparative electrocatalysts.

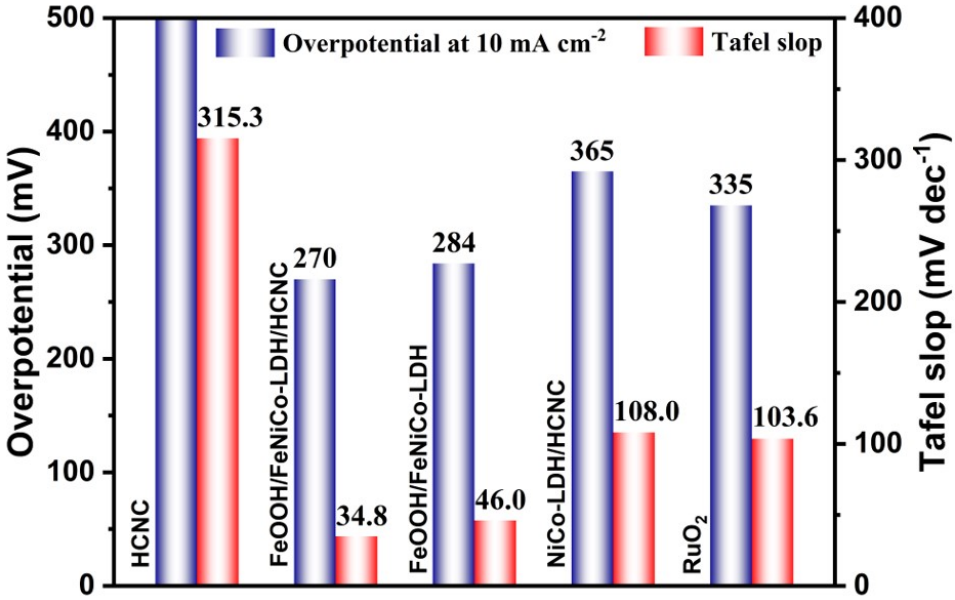

Fig. S18. Overpotentials at current density of 10 mA cm^{-2} and Tafel slopes for OER in 1.0 M KOH + 0.5 M NaCl of FeOOH/FeNiCo-LDH/HCNC and its comparative electrocatalysts.

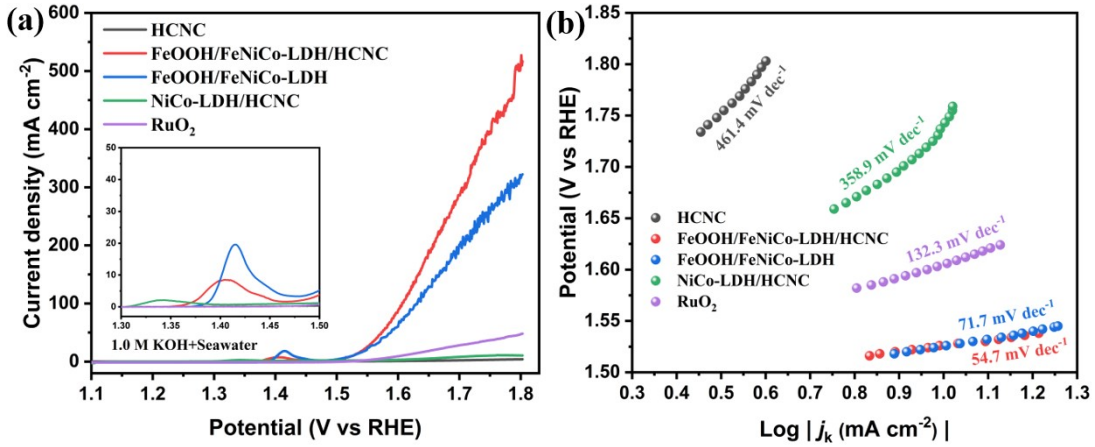

Fig. 19. (a) LSV curves and (b) corresponding Tafel plots for OER in 1.0 M KOH + seawater of FeOOH/FeNiCo-LDH/HCNC and its comparative electrocatalysts.

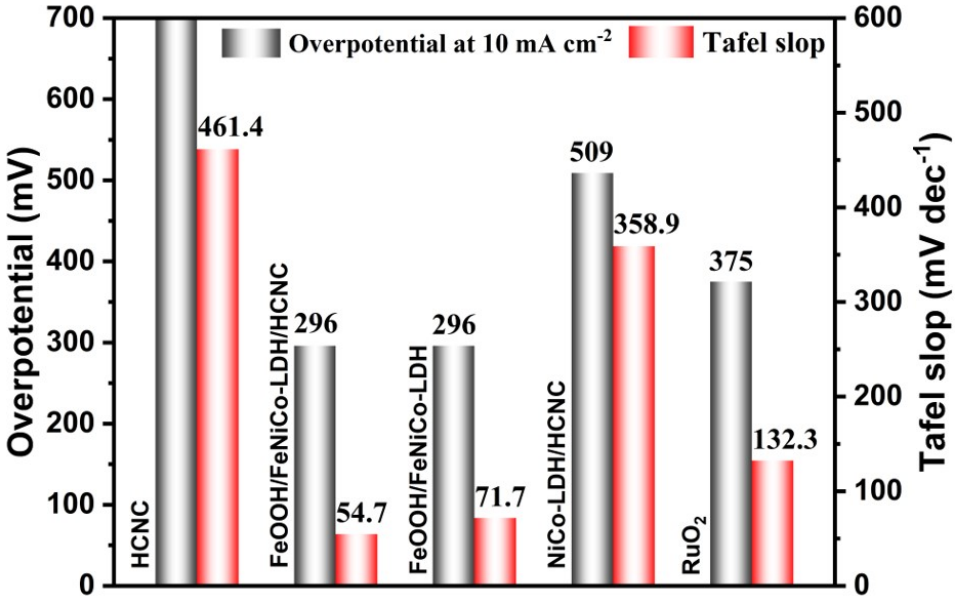

Fig. S20. Overpotentials at current density of 10 mA cm^{-2} and Tafel slopes for OER in 1.0 M KOH + seawater of FeOOH/FeNiCo-LDH/HCNC and its comparative electrocatalysts.

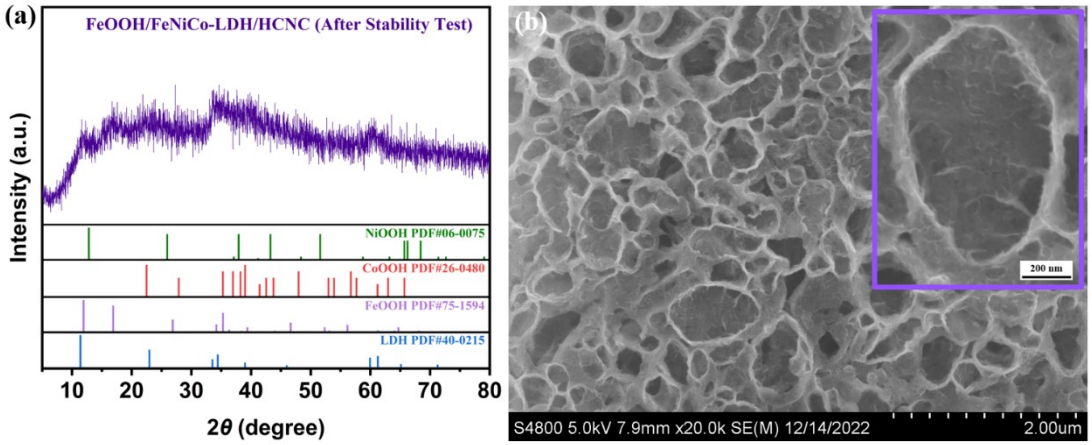

Fig. S21. (a) XRD pattern and (b) SEM image of FeOOH/FeNiCo-LDH/HCNC after OER stability test.

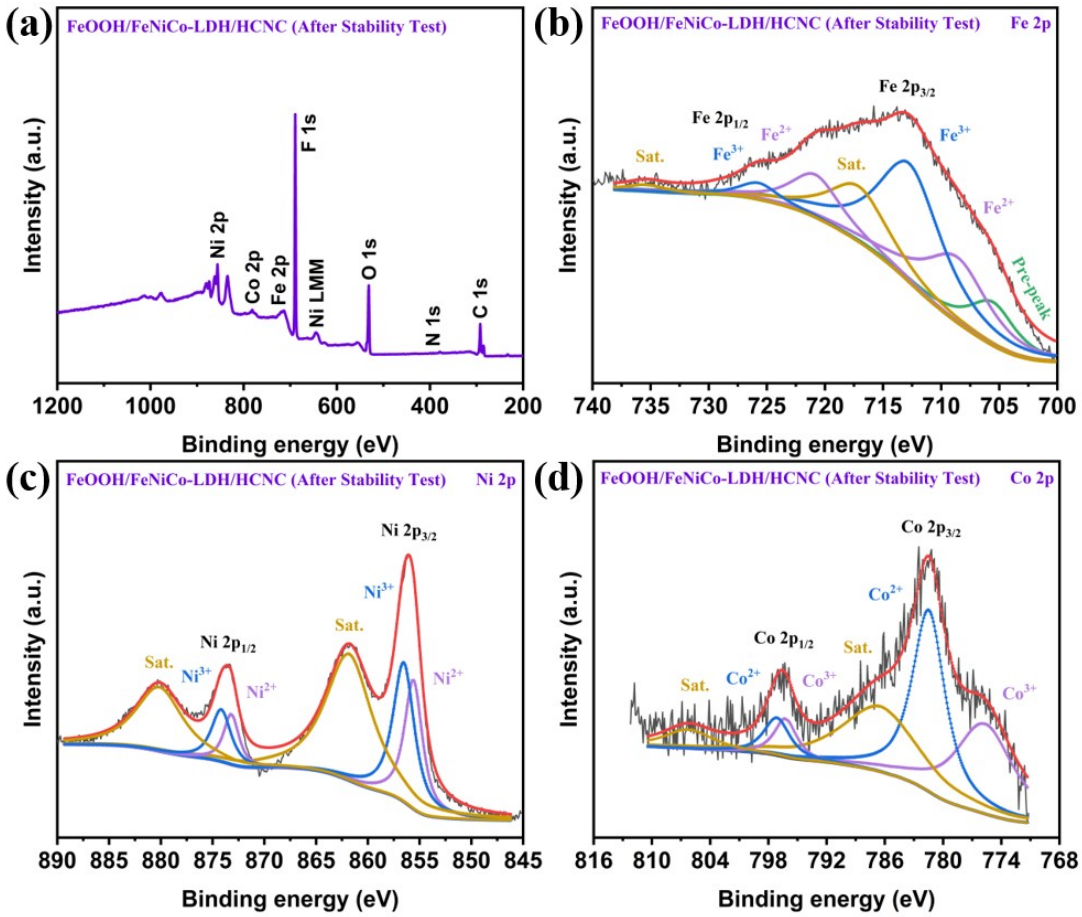

Fig. S22. (a) Survey XPS spectra of FeOOH/FeNiCo-LDH/HCNC after OER stability test. High-resolution XPS spectra of (b) Fe 2p, (c) Ni 2p, and (d) Co 2p in FeOOH/FeNiCo-LDH/HCNC after OER stability test.

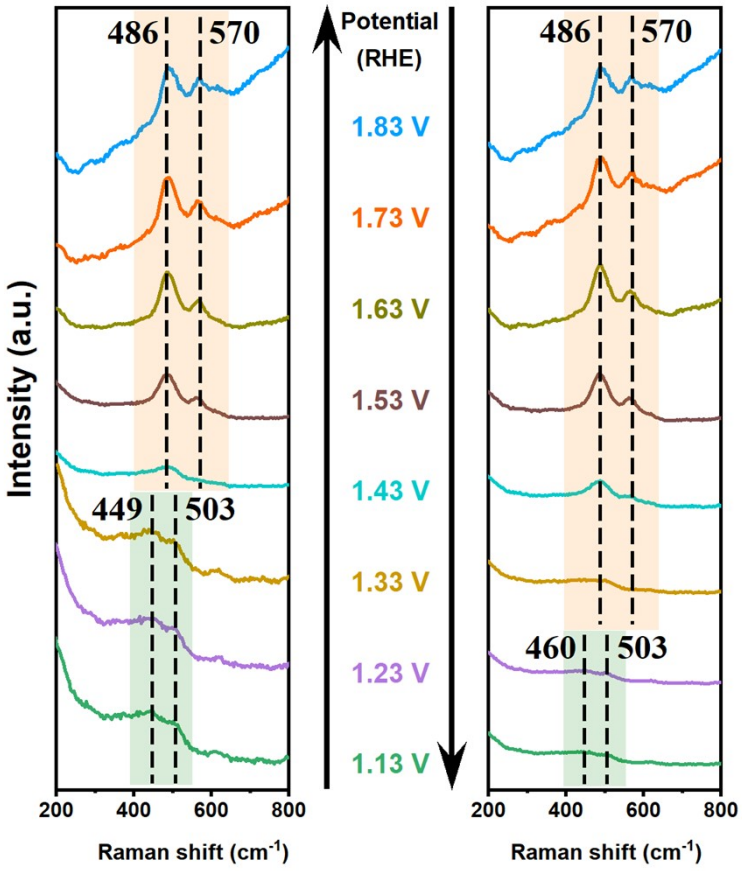

Fig. S23. In-situ Raman spectra of NiCo-LDH/HCNC during OER in 1.0 M KOH.

The *in-situ* Raman characterization of NiCo-LDH/HCNC during OER was conducted under the same conditions as FeOOH/FeNiCo-LDH/HCNC. As displayed in **Fig. S23**, during the potential increase process, the pristine Raman peaks at 449 and 503 cm^{-1} (NiII/CoII-O in LDH) transformed into new peaks at 486 and 570 cm^{-1} (NiCoOOH). In the subsequent decrease process, the Raman peaks assigned to NiCoOOH gradually weakens and reversibly returns to NiCo-LDH. Thus, NiCo-LDH/HCNC undergoes the reversible phase reconstruction to form unstable NiCoOOH species during OER.

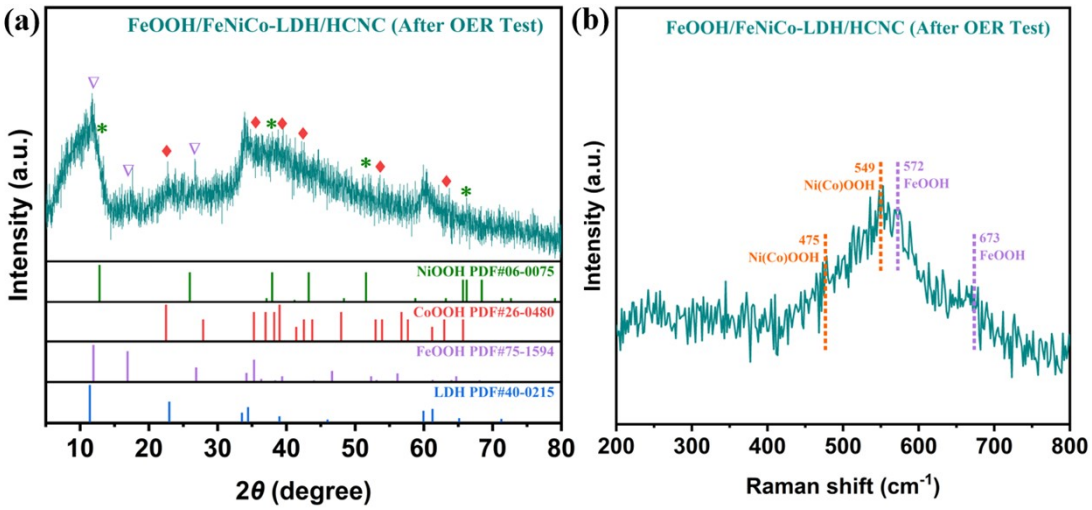

Fig. S24. (a) XRD pattern and (b) Raman spectra of FeOOH/FeNiCo-LDH/HCNC after OER test.

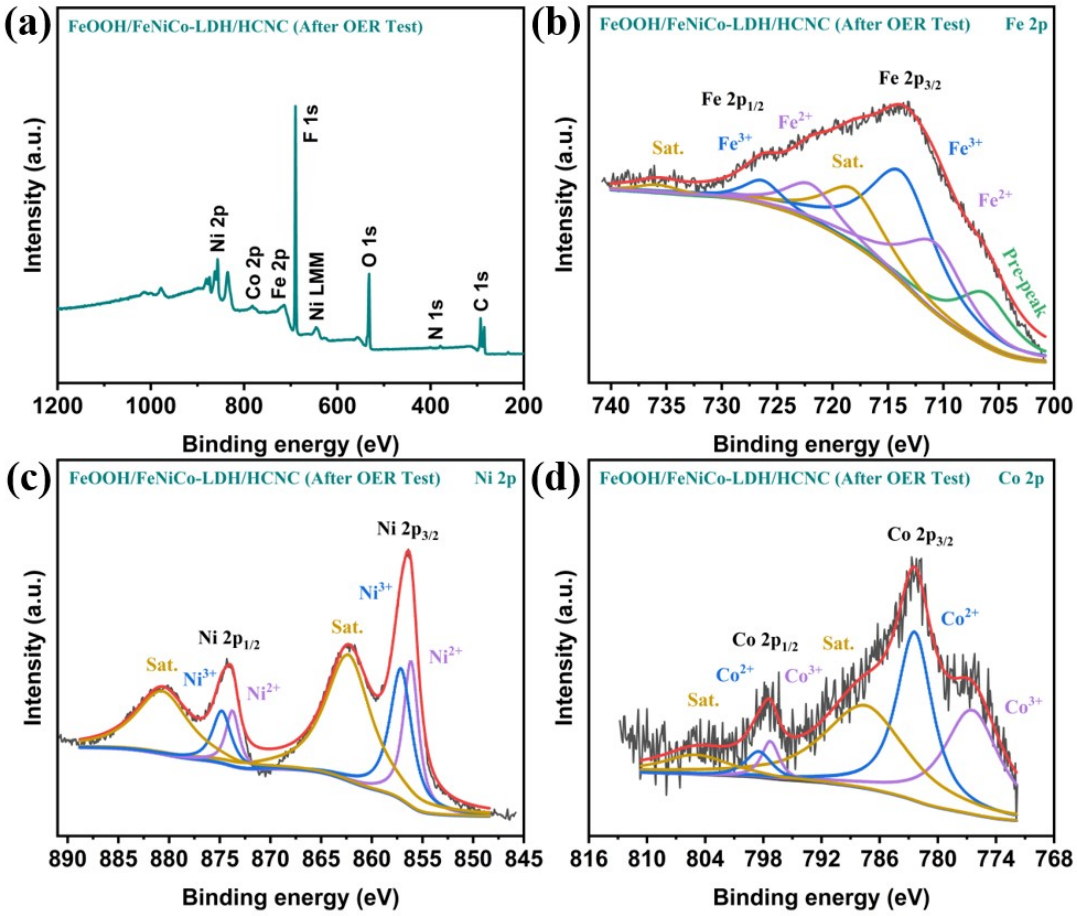

Fig. S25. (a) Survey XPS spectra of FeOOH/FeNiCo-LDH/HCNC after OER test. High-resolution XPS spectra of (b) Fe 2p, (c) Ni 2p, and (d) Co 2p in FeOOH/FeNiCo-LDH/HCNC after OER test.

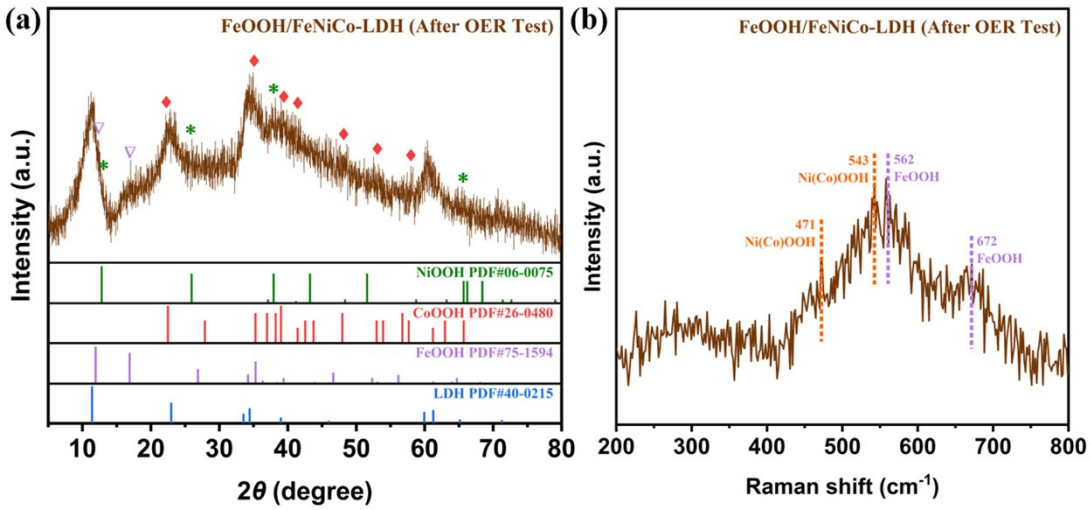

Fig. S26. (a) XRD pattern and (b) Raman spectra of FeOOH/FeNiCo-LDH after OER test.

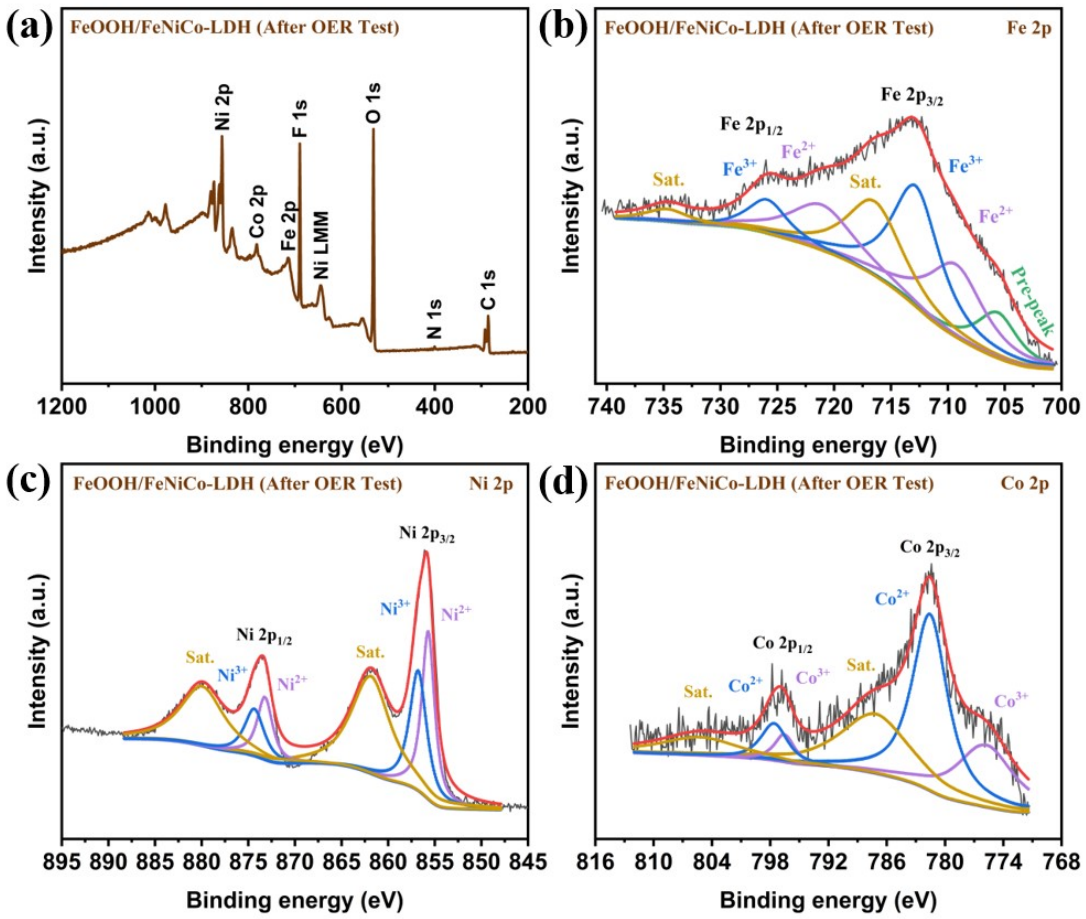

Fig. S27. (a) Survey XPS spectra of FeOOH/FeNiCo-LDH after OER test. High-resolution XPS spectra of (b) Fe 2p, (c) Ni 2p, and (d) Co 2p in FeOOH/FeNiCo-LDH after OER test.

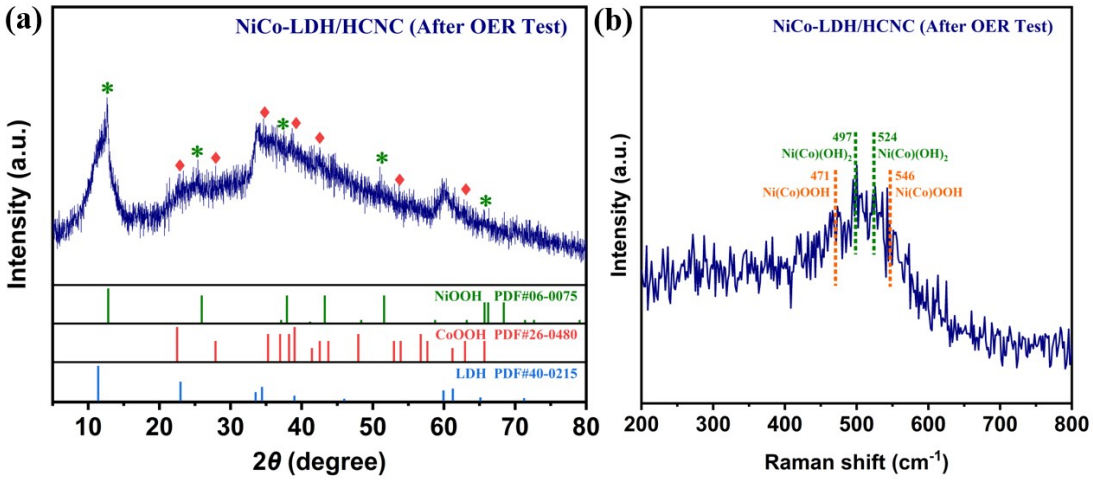

Fig. S28. (a) XRD pattern and (b) Raman spectra of NiCo-LDH/HCNC after OER test.

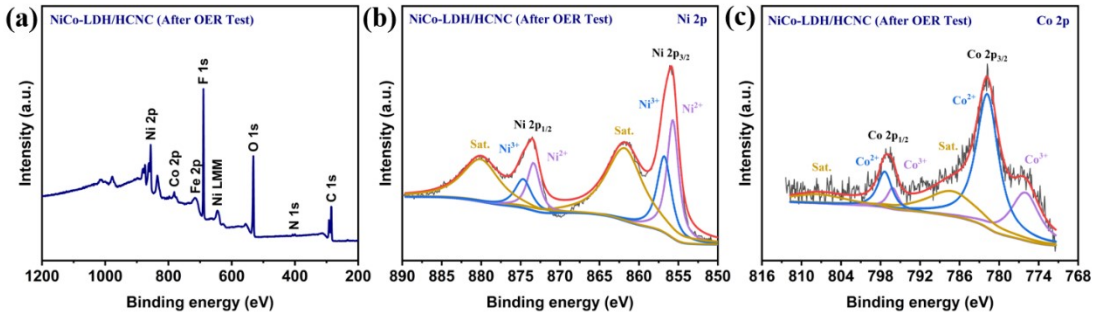

Fig. S29. (a) Survey XPS spectra of NiCo-LDH/HCNC after OER test. High-resolution XPS spectra of (b) Ni 2p and (c) Co 2p in NiCo-LDH/HCNC after OER test.

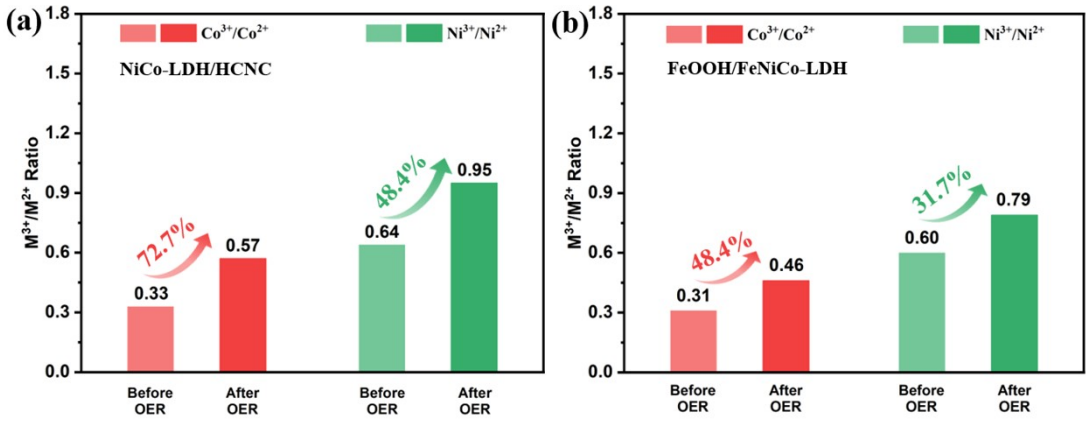

Fig. S30. M^{3+}/M^{2+} ratios in (a) NiCo-LDH/HCNC and (b) FeOOH/FeNiCo-LDH before/after OER test.

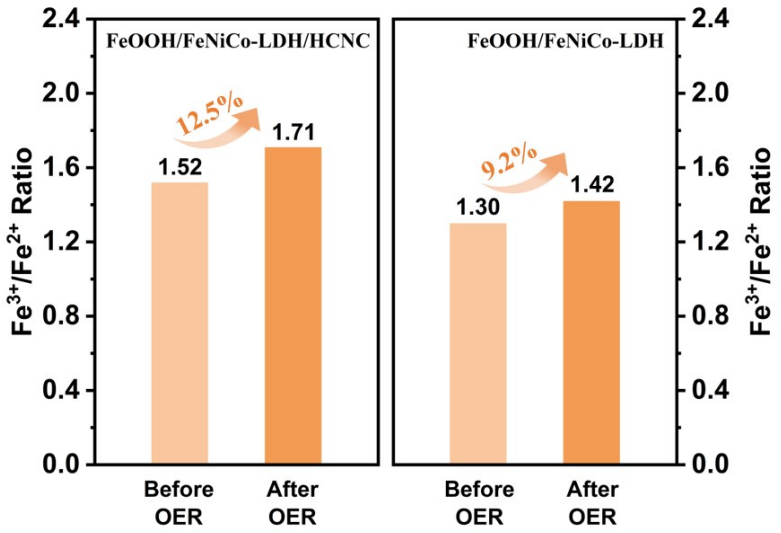

Fig. S31. Fe^{3+}/Fe^{2+} ratios in FeOOH/FeNiCo-LDH/HCNC and FeOOH/FeNiCo-LDH before/after OER test.

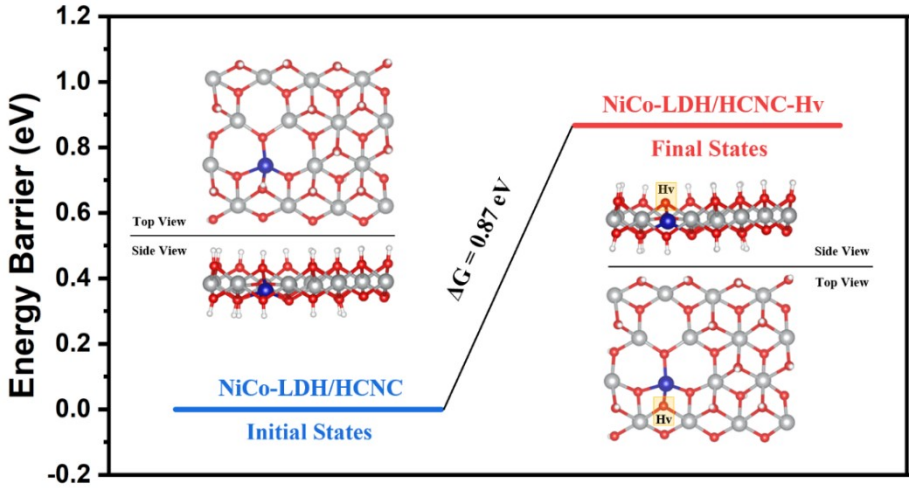

Fig. S32. Calculated energy barrier for the dehydrogenation of NiCo-LDH/HCNC.

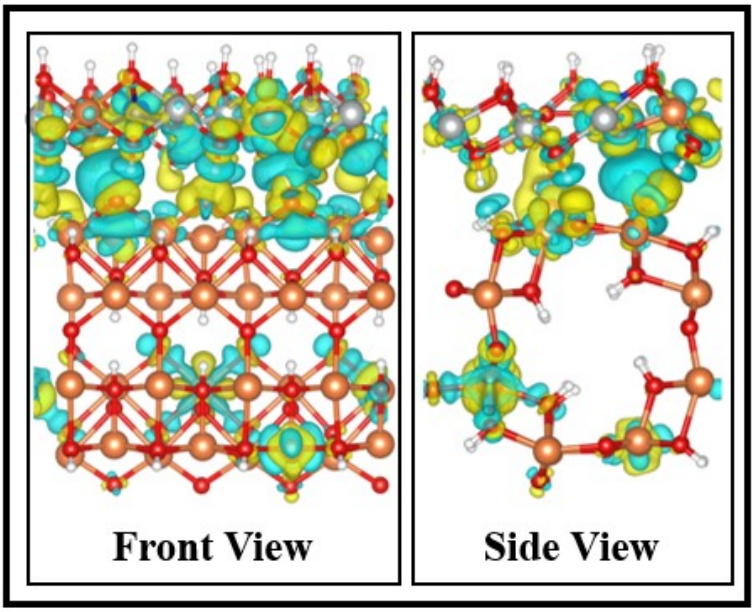

Fig. S33. Charge density difference of FeOOH/FeNiCo-LDH before and after the introduction of FeOOH (Isosurface level was set at 0.02 e $Å^{-3}$; The charge accumulation and depletion are denoted by yellow and blue colors, respectively).

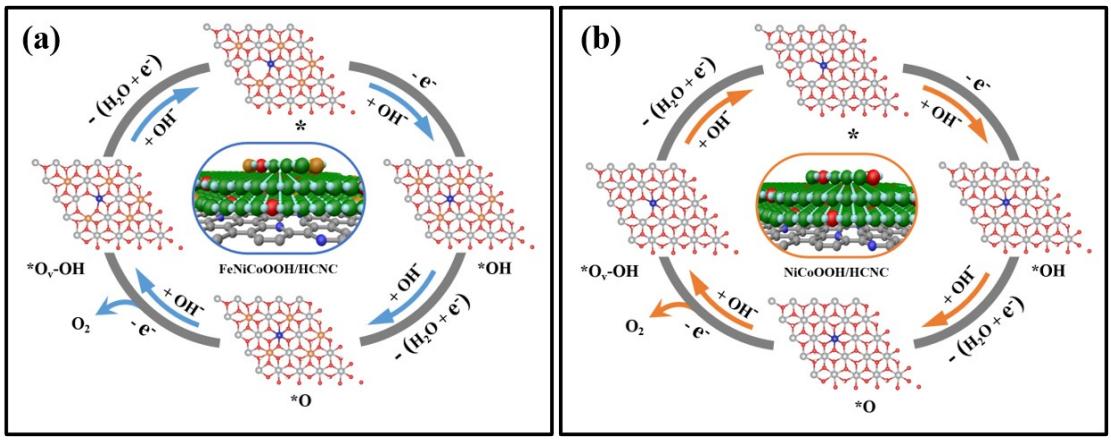

Fig. S34. OER pathway with the formation of *OH, *O, and *O_v-OH intermediates (* represents active site) on (a) FeNiCoOOH and (b) NiCoOOH.

Table S1. ICP-OES of NiCo-LDH/HCNC, FeOOH/FeNiCo-LDH, and FeOOH/FeNiCo-LDH/HCNC.

Samples	Fe (wt%)	Ni (wt%)	Co (wt%)
FeOOH/FeNiCo-LDH/HCNC	7.25	30.02	1.40
FeOOH/FeNiCo-LDH	6.32	40.62	3.19
NiCo-LDH/HCNC	—	33.88	2.16

Table S2. Binding energies of Ni 2p in FeOOH/FeNiCo-LDH/HCNC and its comparative samples.

	Ni $2p_{3/2}$			Ni $2p_{1/2}$		
	Ni^{2+}	Ni^{3+}	Sat.	Ni^{2+}	Ni^{3+}	Sat.
FeOOH/FeNiCo-LDH/HCNC	856.4	857.5	862.2	874.0	875.4	880.4
FeOOH/FeNiCo-LDH	856.2	857.3	862.0	873.9	875.1	880.2
NiCo-LDH/HCNC	856.1	857.1	861.9	873.8	874.9	880.1

Table S3. Binding energies of Co 2p in FeOOH/FeNiCo-LDH/HCNC and its comparative samples.

	Co $2p_{3/2}$			Co $2p_{1/2}$		
	Co^{3+}	Co^{2+}	Sat.	Co^{3+}	Co^{2+}	Sat.
FeOOH/FeNiCo-LDH/HCNC	776.4	782.4	788.4	797.4	798.5	805.1
FeOOH/FeNiCo-LDH	776.2	782.1	786.8	796.8	797.8	804.3
NiCo-LDH/HCNC	776.1	782.0	788.6	796.5	797.8	804.8

Table S4. Comparison of the electrocatalytic performance for OER of various electrocatalysts in 1.0 M KOH electrolyte.

Electrocatalysts	Substrate*	Tafel (mV dec^{-1})	η10 (mV)	η100 (mV)	Ref.
(Fe,Co)OOH/MI	NF	73	230	290	Adv. Mater. 2022, 34, 2200270
B-$CoSe_2$@CoNi LDH HNA	CC	55	240	320	Adv. Sci. 2022, 9, 2104522
S-FeOOH/IF	IF	59	244	308	Adv. Funct. Mater. 2022, 32, 2112674
Co-C@NiFe LDH	GC	57.9	249	328	Chem. Eng. J. 2021, 415, 128879
$H_2PO_2^-$/FeNi-LDH-V_2C	GC	46.5	250	310	Appl. Catal. B 2021, 297, 120474
Co@NiFe-LDH	GC	44	253	320	J. Mater. Chem. A 2022, 10, 5244
CoNiRu-NT	NF	67	255(20)	335	Adv. Mater. 2022, 34, 2107488
CoNiFe-LDH Nanocages	GC	31.4	257	350	Adv. Funct. Mater. 2023, 2300808
FeOOH/FeNiCo-LDH/HCNC	**GC**	**32.4**	**258**	**299**	**This work**
CN-5Fe HMs	GC	48.7	258	340	Adv. Funct. Mater. 2022, 32, 2200726
Mo-NiCo LDHs(Vo)	NF	94.5	258	361	Chem. Eng. J. 2023, 463, 142396
NiFeCe-LDH/MXene	GC	42.8	260	470	J. Energy Chem. 2021, 52, 412
Ni_3S_4@CoFe-LDH	GC	70.2	262	—	J. Mater. Chem. A 2023, 11, 16349
CoVRu LDH	NF	74.5	263(25)	325	Chem. Eng. J. 2023, 452, 139151
NiCo LDH-TPA	GF	52.4	267	—	Angew. Chem. Int. Ed. 2021, 60, 10614
FeCoNi-LDHs	GC	42.34	269	—	Adv. Energy Mater. 2021, 11, 2102141
$Co_{0.50}Fe_{0.50}$- LDH	CC	64.6	270	359	ACS Catal. 2023, 13, 1477
Ag NW@NiMnLDH	GC	40.2	270	—	ACS Nano 2020, 14, 1770
Ni-Fe LDH(60%)/H-$Ti_3C_2T_x$	GC	47	270(20)	364	Carbon 2023, 212, 118141
NFO/3DGN-10	NF	64	272	—	Carbon 2022, 200, 422
Ru@NiV-LDH	CC	60	272	—	J. Mater. Chem. A 2022, 10, 3618
NiCoFe-HO@NiCo-LDH YSMRs	GC	49.7	278	360	Angew. Chem. Int. Ed. 2022, 61, e202213049
ZnCoCH@$Ti_3C_2T_x$	GC	46.2	280	—	Chem. Eng. J. 2023, 456, 141041
Ni-Fe LDH Hollow Nanoprisms	GC	49.4	280	330	Angew. Chem. Int. Ed. 2018, 57, 172
γ-FeOOH/NF-6M	NF	51	286	316	Adv. Mater. 2021, 33, 2005587
$NiCo_2S_4$@NiFe LDH	GC	86.4	287	—	Appl. Catal. B 2021, 286, 119869
NiCo-LDH/GO-CNTs	GC	66.8	290	—	Nano Res. 2021, 14, 4783
FeCoNi-ATNs/NF	NF	52.7	295	360	Adv. Energy Mater. 2019, 9, 1901312
NiFe-LDH/Fe_1-N-C	GC	41	320	—	Adv. Energy Mater. 2023, 13, 2203609
5% Ce-doped Co-Ni LDH	GC	130	340	—	ACS Catal. 2023, 13, 4799

* Glassy carbon (GC), Carbon cloth (CC), Carbon paper (CP), Iron foam (IF), Nickel foam (NF), Graphene foam (GF).

Table S5. Comparison of the electrocatalytic performance for OER of various electrocatalysts in 1.0 M KOH + 0.5 M NaCl or 1.0 M KOH + seawater electrolytes.

Electrocatalysts	Substrate*	Electrolyte	Tafel (mV dec^{-1})	η10 (mV)	η100 (mV)	Ref.
FeOOH/FeNiCo-LDH/HCNC	**GC**	**1.0 M KOH 0.5 M NaCl**	**34.8**	**270**	**316**	**This work**
		1.0 M KOH Seawater	**54.7**	**296**	**377**	
NiCoHPi@Ni_3N/NF	NF	1.0 M KOH 0.5 M NaCl	80.8	310(20)	365	ACS Appl. Mater. Interfaces 2022, 14, 22061
		1.0 M KOH Seawater	108.6	325(20)	396	
(Ni, Fe)OOH@Ni_xP	NF	1.0 M KOH 0.5 M NaCl	34	216	252	Appl. Catal. B 2023, 336, 122926
		1.0 M KOH Seawater	44	216	262	
S-(Ni,Fe)OOH	NF	1.0 M KOH 0.5 M NaCl	—	—	278	Energy Environ. Sci. 2020, 13, 3439
		1.0 M KOH Seawater	—	—	300	
NiIr-LDH	NF	1.0 M KOH 0.5 M NaCl	60.5	—	286	J. Am. Chem. Soc. 2022, 144, 9254
		1.0 M KOH Seawater	78.8	—	315	
0.5Fe-$NiCo_2O_4$@CC	CC	1.0 M KOH 0.5 M NaCl	76.7	273	330	Small 2022, 18, 2106187
		1.0 M KOH Seawater	76.1	293	360	
Co-N,P-HCS	NF	1.0 M KOH Seawater	121.5	320	490	Adv. Mater. 2022, 34, 2204021
Ni_2P-Fe_2P/NF	NF	1.0 M KOH Seawater	—	240	305	Adv. Funct. Mater. 2020, 31, 2006484
CoP_x@FeOOH	NF	1.0 M KOH Seawater	50.3	235	283	Appl. Catal. B 2021, 294, 120256
$Co_{1.98}$-NiFe LDH	CFP	1.0 M KOH 0.5 M NaCl	—	254(20)	309	Appl. Catal. B 2022, 314, 121491
Pt-CoFe(II) LDHs	NF	1.0 M KOH Seawater	—	239	302	J. Power Sources 2022, 532, 231353
B-Co_2Fe LDH	NF	1.0 M KOH Seawater	63.8	245	310	Nano Energy 2021, 83, 105838
Fe-$Ni(OH)_2$/Ni_3S_2@NF	NF	1.0 M KOH 0.5 M NaCl	46	269	320	Nano Res. 2021, 14, 1149

* Glassy carbon (GC), Cu foil (CF), Nickel foam (NF), Carbon fiber paper (CFP), Nickel-iron foam (NFF), Carbon cloth (CC).

Table S6. Comparison of AEM performance for water electrolysis of various electrocatalysts in 1.0 M KOH electrolyte.

Electrocatalysts	Temp. (℃)	Area (cm^{-2})	Electrolyte	Stability (mA cm^{-2}@V)	Degradation Rate	Ref
FeOOH/FeNiCo-LDH/HCNC	**65**	**1**	**1.0 M KOH**	**500@1.95**	**1.7 mV/h (120 h)**	**This work**
NiCoO-NiCo/C	50	64	1.0 M KOH	440@1.85	4.6 mV/h (10 h)	Appl. Catal. B 2021, 292, 120170
Fe_2O_3/$NiSe_2$-FeOOH/NF	25	2	1.0 M KOH	500@1.80	1.5 mV/h (75 h)	Appl. Catal. B 2024, 355, 124148
NiFeCr-LDH	40	1.2	1.0 M KOH	1000@2.11	(50 h)	Small 2022, 18, 2200303
Ni_2P/Ni_7S_6	75	1	1.0 M KOH	1000@2.50	1.9 mV/h (140 h)	Appl. Catal. B 2023, 330, 122633
Ni_3S_2/Cr_2S_3@NF	60	1.2	3.0 M KOH	1000@2.16	1.7 mV/h (35 h)	J. Am. Chem. Soc. 2022, 144, 6028
FeNiPt@C	60	4	1.0 M KOH	200@1.67	1.1 mV/h (110 h)	Adv. Sci. 2024, 11, 2308205
RuZn-Co_3O_4	60	4	1.0 M KOH	500@1.75	1.3 mV/h (100 h)	Angew. Chem. Int. Ed. 2024, e202407509
$L_2S_2N_1F_2$	60	3.8	1.0 M KOH	500@1.70	3.0 mV/h (40 h)	Chem. Eng. J. 2023, 452, 139105
$(FeCoNiCrMnCu)_3O_4$	50	1	1.0 M NaOH	500@1.68	2.0 mV/h (40 h)	ACS Materials Lett. 2024, 6, 1739
F-TMO	70	5	Pure water	500@1.82	2.5 mV/h (336 h)	ACS Nano 2024, 18, 22454
FePi-NiS/NF	50	25	1.0 M KOH	500@1.87	3.0 mV/h (30 h)	Appl. Catal. B 2024, 340, 123252
d-(Fe,Ni)OOH	73	25	1.0 M KOH	500@1.80	(96 h)	Adv. Mater. 2023, 35, 2306097
NiFe LDH/NiS	85	20	30% KOH	400@2.02	(80 h)	Adv. Energy Mater. 2021, 11, 2102353
NiCoFe-NDA	50	4	0.1 M KOH	325@1.80	(75 h)	Energy Environ. Sci. 2021, 14, 6546
Co, Mo-NiFe LDH	85	4	30% KOH	500@1.94	(130 h)	Adv. Energy Mater. 2023, 13, 2203595
Fe/S-NiOOH	60	1	1.0 M KOH	1000@2.65	(100 h)	Small 2024, 2310064

CoCrOx	60	5	1.0 M KOH	500@2.00	(120 h)	Nat. Commun. 2024, 15, 3416

Reference

[S1] J. Hafner, J. Comput. Chem., 2008, 29, 2044-2078.

[S2] P. E. Blöchl, Phys. Rev. B, 1994, 50, 17953-17979.

[S3] J. P. Perdew and K. Burke, Phys. Rev. Lett., 1996, 77, 3865-3868.

[S4] S. Grimme, J. Comput. Chem., 2006, 27, 1787-1799.

[S5] H. J. Monkhorst and J. D. Pack, Phys. Rev. B, 1976, 13, 5188-5192.

[S6] V. I. Anisimov, J. Zaanen and O. K. Andersen, Phys. Rev. B, 1991, 44, 943-954.

[S7] V. I. Anisimov, F. Aryasetiawan and A. I. Lichtenstein, J. Phys. Condens. Matter, 1997, 9, 767-808.

[S8] L. Wang, T. Maxisch and G. Ceder, Phys. Rev. B, 2006, 73, 195107.

[S9] E. Skúlason, G. S. Karlberg, J. Rossmeisl, T. Bligaard, J. Greeley, H. Jónsson and J. K. Nørskov, Phys. Chem. Chem. Phys., 2007, 9, 3241-3250.

[S10] B. Zhang, X. Zheng, O. Voznyy, R. Comin, M. Bajdich, M. García-Melchor, L. Han, J. Xu, M. Liu, L. Zheng, F. P. G. de Arquer, C. T. Dinh, F. Fan, M. Yuan, E. Yassitepe, N. Chen, T. Regier, P. Liu, Y. Li, P. De Luna, A. Janmohamed, H. L. Xin, H. Yang, A. Vojvodic and E. H. Sargent, Science, 2016, 352, 333-337.

[S11] W. M. Haynes, D. R. Lide and T. J. Bruno, CRC handbook of chemistry and physics 97th Edition, 2016.

[S12] V. Wang, N. Xu, J.-C. Liu, G. Tang and W.-T. Geng, Comput. Phys. Commun., 2021, 267, 108033.